

Internal Stress Formation and Changes in Oxide Films on a Lead Alloy Anode Surface

Jianzhong Li^{1,2,*}, Yunkai Wang^{1,2}, Ying Bi^{1,2}, Ying Li^{1,2}, Yanwen Tian^{1,2}

¹ School of Metallurgy, Northeastern University, Shenyang 110819, China

² Liaoning Key Laboratory for Metallurgical Sensors and Technology, Northeastern University, Shenyang 110819, China

*E-mail: lijz@smm.neu.edu.cn

Received: 26 July 2016 / Accepted: 21 September 2016 / Published: 10 November 2016

Internal stresses significantly influence the mechanical, structural, and electrochemical performance of oxide films on lead alloy substrates. In this study, internal stress formation and changes on oxide films formed *in situ* on a lead anode surface were evaluated with Raman spectroscopy. The results showed that stress changes were highly dependent upon the morphology and phase composition of the oxide film, as determined by scanning electron microscopy and X-ray diffraction. PbO/PbO₂ films generated in the chromium(VI) electrolyte obviously induced compressive stress in the initial oxidation stage, followed by tensile stress. However, PbO/PbO₂ films obtained using SO₄²⁻ and Cl⁻ electrolytes were attributed to the influence tensile stress over the entire oxidation time. PbCrO₄ and PbSO₄ films compositions contributed to the development of compressive stress. The coupling of changes in compressive and tensile stresses on oxide films tended to generate microcracks, leading to an increase in the electrical conductivity of the films.

Keywords: Internal stresses; lead substrate; anode; oxide films; oxidation

1. INTRODUCTION

Most recent attention and industrial practices using anodic materials has involved inert substrates, such as titanium, carbon, or PbO replacement coatings (e.g., dimensionally stable anode or boron-doped diamond) [1]. Lead alloy anodes are still widely used in industrial applications, such as chromium plating [2], electrochemical surface passivation [3], lead/acid batteries [4-5], and hydrometallurgical processes (e.g., copper electrowinning) [6-7], due to their good castability and mechanical properties, low corrosion rates, high electrocatalytic efficiency, and good conductivity of the contact layer [8-9]. In these applications, lead alloy anodes undergo high current densities in

aggressive environments, such as H_2SO_4 , chromium(VI), or chlorine-containing solutions. The layer of PbO or PbO_2 found on lead substrate anode surfaces during use is essential because it is the electrochemically active component of the anode. After practical application, the dioxide layer has a tendency to crack or break away from the lead alloy anode surface, exposing a fresh layer of lead to the electrolyte. Although these attractive properties have been a driving force for earlier studies and applications limited to coatings formed *in situ* on lead or lead alloys, anodes of this type suffer from continuous corrosion of the underlying lead substrate. Moreover, previous studies assessed anode corrosion resistance and mechanical properties by changing the coating composition and anodic dissolution rate [9-12], leading to a systematic underestimation of the contribution of coating stress changes.

When oxide films are thin (about several hundred nm), crystal growth is maintained in the same direction as the anode substrate material, such as titanium alloy, stainless steel, and lead alloy [13]. However, prolonged oxidation induces excessive growth of the oxide film which produces a lattice constant that is inconsistent with the initial film, thereby generating internal stress. Meanwhile, interface lattice growth and the anode substrate may produce residual stress if there is a large mismatch between the thermal, structural, and mechanical properties of the substrate and overlay material [14-15]. As the oxidation proceeds, structural changes in the oxide film on the anode surface results in a corresponding change in lattice constant, leading to a change in the stresses generated. Thus, shear stress on the film interface develops whether the thin film stresses are compressive or tensile. As a result, the oxide film may show microcracks, folds, or even fall off, especially on lead alloy anodes, when the stresses increase to overcome the shear stress. Consequently, the life of the anode is shortened. Clearly, stress changes and residual stress play an important role in the cracking, spalling, and bonding behavior of engineered surfaces [16].

Factors affecting stress changes and residual stress of oxide films on lead alloy anodes are very complex and erratic, encompassing not only substrate composition, purity, metallurgy, microstructure, and thermal history, but also electrolyte solutions, duration, and process parameters [1, 10, 16]. All of these factors make it very difficult to assess stress changes and residual stresses. In the current study, oxide films were formed *in situ* on a lead anode and their stress changes analyzed with particular emphasis on different ionic electrolyte solutions by means of Raman spectroscopy and X-ray diffraction (XRD). In order to avoid experimental error, a certain alloy component of lead alloy anode materials has been assessed in this study

2. EXPERIMENTAL METHODS

2.1 Preparation of oxide films

Commercial lead alloy anode materials were used as research samples (anode contents, Pb -1 wt% Ca), and anode substrates were $20 \times 10 \times 7$ mm. Anodes were mechanically polished with emery paper up to 1200 grit to ensure similar surface roughness, thoroughly cleaned in acetone and deionized water before drying, and then placed in dry container for later use. In order to study internal formation and change of different stresses on oxide films grown on the lead anode surface

during the initial period, the same set of electrolysis experiments were carried out after 1, 5, 10, and 20 min of oxidation time. The electrolyte solutions used included $0.4 \text{ mol}\cdot\text{L}^{-1} \text{ SO}_4^{2-}$, $1.0 \text{ mol}\cdot\text{L}^{-1} \text{ Cl}^-$, and $1.5 \text{ mol}\cdot\text{L}^{-1}$ chromium (VI) (Using CrO_3 as source of chromium; solvent used by deionized water) to simulate plating solutions under at 40°C . The lead alloy was used as the working electrode for preparing the oxide films. Low-carbon steel was used as a counter electrode for building the electrolysis system. During all electrolysis experiments, the current density was fixed at $20 \text{ A}\cdot\text{dm}^{-2}$ to avoid experimental error. After washing in deionized water and rapidly drying, lead anode samples with different oxide films were obtained under different conditions.

2.2 Property tests

A Zeiss/EVO18 scanning electron microscope (SEM) was used to characterize the surface morphology and structure of the oxide films. The phase purity and crystal structure of the synthesized samples were analyzed using a Rigaku/Ultima IV K- α radiation source ($\lambda = 0.154056 \text{ nm}$, 40 kV , 200 mA) in a 2θ range of 10° to 80° with a scanning speed of $1^\circ\cdot\text{min}^{-1}$. To evaluate the evolution of interfacial stresses at the oxide film-substrate interface, residual stresses on lead alloy substrates were determined using the $\sin^2\psi$ technique via XRD. Details of the XRD procedure have been described previously [16]. The XRD method used was based on elastic deformation of the polycrystalline material to measure residual stress. With this method, the residual stresses for an original lead alloy substrate in the present work were determined to be -3.83 MPa . Residual stresses were determined based on measurement of the diffraction peak for different ψ angles; ψ is the angle between the normal of the sample and normal to the diffracting plane. This technique was required the films to be compact, with a thickness greater than $2 \mu\text{m}$ on the anode surface. Otherwise, the evolution of the stresses on the oxide films were assessed using a Raman spectroscopic method suitable for oxide films [17].

Raman data were obtained with a Jobin Yvon HR800 Raman spectrometer system equipped with a 633 nm He-Ne laser. The power of the excitation laser at the sample position was 17 mW . Scattered radiation from the sample passed through a SPEX Triplemate monochromator and was detected by an OMAIII optical multichannel analyzer with a photodiode array thermoelectrically cooled to -35°C . The samples were pressed into self-supporting wafers and recorded at room temperature via long-focus lens. Each sample was scanned three times. Figures with a peak position error less than $\pm 1 \text{ cm}^{-1}$ were considered in this research. In addition, Raman spectra for the assessment of residual stress were correlated with the $\sin^2\psi$ technique through XRD using and oxide film thicknesses greater than $2 \mu\text{m}$.

The electrical conductivity of the oxide films in all cases were characterized using an electrochemical alternating current impedance test. Alternating current impedance measurements were performed in a conventional 250-mL , three-compartment, Pyrex cell using an electrochemical workstation, model PARSTAT 2273 (American Princeton Co.). A defined sample area of 2 cm^2 was exposed to the electrolyte, and the current was normalized to the geometrical surface area. A Luggin capillary was placed near the working electrode to minimize solution resistance. Platinum foil was used as a counter electrode for evaluating the electrochemical properties of the oxide films, and a

saturated calomel electrode was used as the reference electrode. All electrode potentials referenced the saturated calomel electrode unless stated otherwise. Electrochemical impedance spectroscopy measurements were performed in a frequency range of 10^5 to 10^{-1} Hz with 10 points per decade, and a *sin* wave with 10 mV amplitude was used to perturb the system. Impedance data were analyzed and fitted with the ZSimpWin equivalent circuit simulation software. All electrochemical tests were carried out in 3.5 wt% NaCl at room temperature to avoid corrosion of the different electrolyte ions over the fixed test time.

3. RESULTS AND DISCUSSION

3.1 Effect of chromium(VI) on internal stress of oxide films on the surface of lead substrate anode

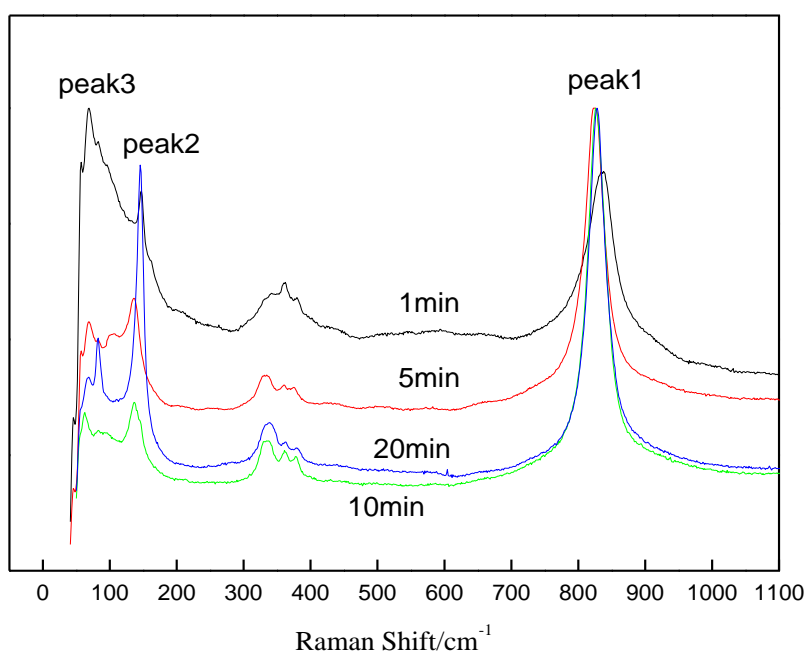


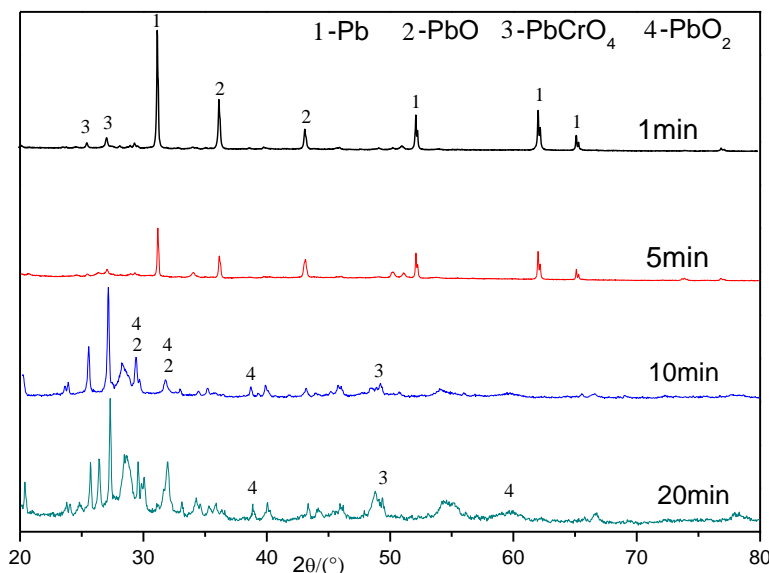
Figure 1. Raman spectra of lead alloy surfaces treated in $1.5 \text{ mol}\cdot\text{L}^{-1}$ chromium (VI) solution at $40 \text{ }^\circ\text{C}$ after 1, 5, 10, and 20 min of oxidation under the current density $20 \text{ A}\cdot\text{dm}^{-2}$.

As mentioned above, anode performance can degrade by grain coarsening, which is highly dependent on oxide film compositions and phase structures. The growth of large grains at the expense of small grains is due to minimization of the Gibbs free surface energy and mainly depends on the grain size and oxidation time. This leads to *in situ* generation of internal stress on the oxide film. In order to study the gradual development of internal stress on oxide films on the lead substrate anode in chromium (VI) solution, samples oxidized for different lengths of time were prepared and studied by Raman, XRD, and SEM. Raman results showed that all of the films contained four peaks/bands (peaks 1-3; Fig. 1) with bands at 60-70, 130-150, 300-400, and $820\text{-}840 \text{ cm}^{-1}$. However, the peaks shifted with a longer oxidation time (Table 1).

Table 1. Raman peak for lead alloy surfaces exposed to $1.5 \text{ mol}\cdot\text{L}^{-1}$ chromium (VI) solution at $40 \text{ }^\circ\text{C}$ after 1, 5, 10, and 20 min of oxidation under the current density $20 \text{ A}\cdot\text{dm}^{-2}$.

Oxidation time(min)	Peak 1		Peak 2		Peak 3	
	Raman bands (cm^{-1})	Residual stresses(MPa)	Raman bands (cm^{-1})	Residual stresses(MPa)	Raman bands(cm^{-1})	Residual stresses(MPa)
0		-3.83		-3.83		--
1	837.6	-0.336	147.2	1.491(for PbO)	68.9	--
5	826.1	-2.751	136.0	-0.861(for PbO)	68.9	--
10	825.6	-2.856	136.2	-0.819(for PbO)	67.8	--
20	827.9	-2.373	145.5	1.134(for PbO)	68.6	--

Peaks at $300\text{-}400 \text{ cm}^{-1}$ that showed a more complex sawtooth shape are not discussed in the current report. When the oxidation time increased from 1 to 5 min, peaks 1 and 2 showed obvious fluctuation from 837.6 to 826.1 cm^{-1} and 147.2 to 136.0 cm^{-1} , respectively, while peak 3 barely changed its position. In contrast, peaks 1 and 2 did not significantly shift when the oxidation time was increased from 5 to 10 min, while peak 3 shifted remarkably from 68.9 to 62.8 cm^{-1} . When the oxidation time was increased from 10 to 20 min, peak 2 shifted from 136.2 to 145.5 cm^{-1} , and peak 3 shifted from 62.8 to 68.6 cm^{-1} . On the other hand, peak 1 only showed a minor shift during this time frame.

**Figure 2.** X-ray diffractograms of lead alloy surfaces treated in $1.5 \text{ mol}\cdot\text{L}^{-1}$ chromium (VI) solution at $40 \text{ }^\circ\text{C}$ after 1, 5, 10, and 20 min of oxidation under the current density $20 \text{ A}\cdot\text{dm}^{-2}$.

The corresponding XRD pattern and SEM of the different oxidation times under the same conditions are shown in Figs. 2 and 3. As the oxidation time of the lead alloy in chromium (VI) solution increased, the diffraction peaks of lead obviously weakened, while those of PbO/PbO₂ were strengthened. For PbO/PbO₂ mixed films, the PbO was the predominant component. However,

monoclinic PbCrO_4 diffraction peaks were relatively strong with longer oxidation times (10 and 20 min) versus shorter ones (1 and 5 min). According to surface morphology presented in Fig. 3, the ball-shaped grains generated on the lead alloy surface gradually grew in size, eventually covering the rod-shaped grains. This indicates the oxide films initially consisted of monoclinic PbCrO_4 and PbO , and then PbCrO_4 and PbO_2 were gradually generated.

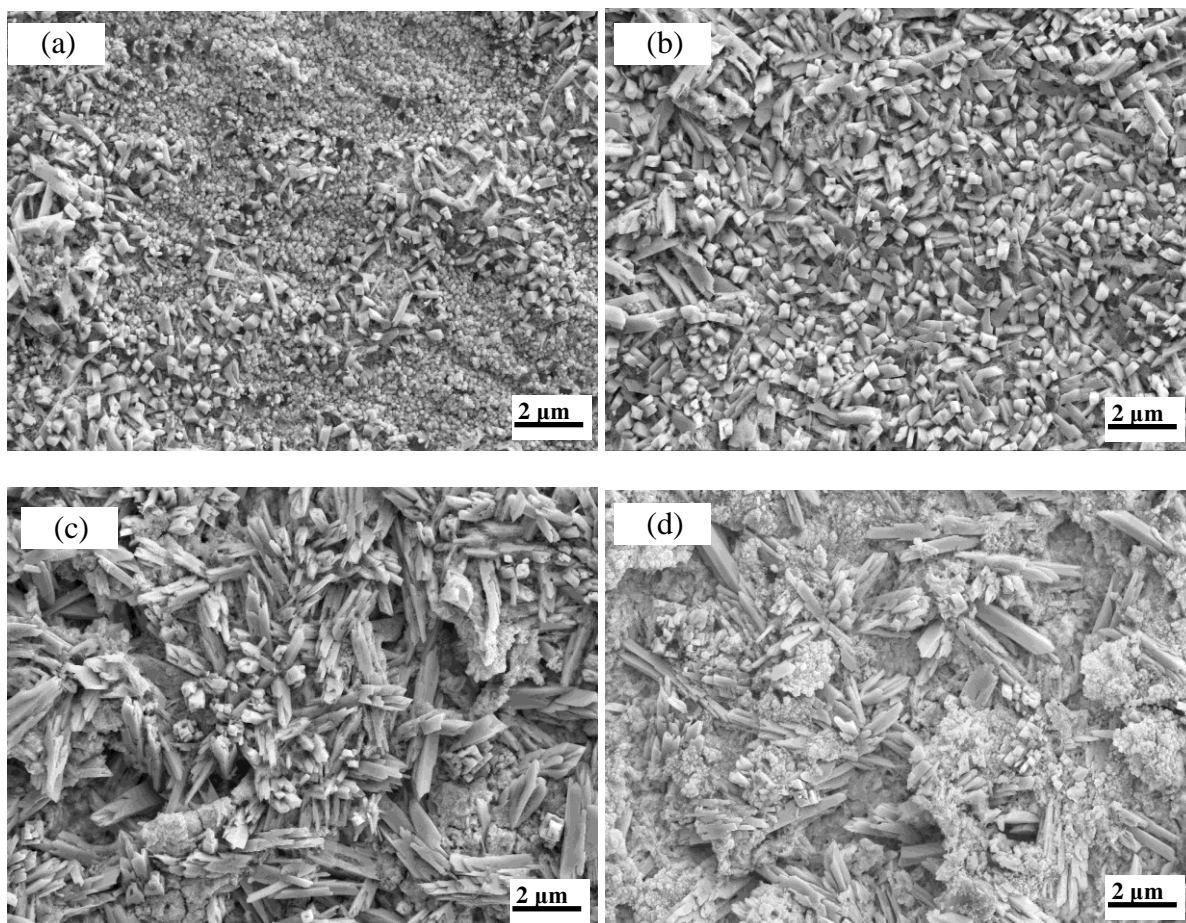


Figure 3. Surface morphology of lead alloy treated in $1.5 \text{ mol}\cdot\text{L}^{-1}$ chromium (VI) solution at $40 \text{ }^\circ\text{C}$ after different oxidation time under the current density $20 \text{ A}\cdot\text{dm}^{-2}$: (a) 1 min, (b) 5 min, (c) 10 min, and (d) 20 min

From the results described above, it appeared that Raman spectral shifts were strongly dependent on crystal structure and morphology, which, in turn, produce different stresses on oxide films grown on lead substrates. Previous reports have shown that peak position deviates from the characteristic frequency with different oxide compositions. In the linear approximation, the deviation in frequency of a given phonon mode (γ) under symmetry-conserving stress can be expressed in terms of the biaxial stresses (σ_{xx}).

$$\sigma_{xx} = \frac{1}{K_\gamma} \Delta W_\gamma = \frac{1}{K_\gamma} (w_s - w_0)$$

σ_{xx} can be calculated according to this stress-deviation relation from the measured Raman frequency shift of a given Raman phonon mode if the coefficient of linear stress (K_γ) is known (4.76

$\text{MPa}^{-1}\cdot\text{cm}^{-1}$) and can be correlated with the $\sin^2\psi$ technique through XRD for oxide film thicknesses greater than $2\ \mu\text{m}$. The standard peak position (w_0) for PbCrO_4 , PbSO_4 , PbO , and PbO_2 were 839.2, 978.3, 140.7, and $133.7\ \text{cm}^{-1}$, respectively, and w_s was the measured peak position. When ΔW_γ is negative, σ_{xx} represents compressive stresses. When ΔW_γ is positive, σ_{xx} represents tensile stress. [17-19]

Li *et al.* [20] reported a fixed PbCrO_4 Raman band at $\sim 836\ \text{cm}^{-1}$ which is similar to our peak 1. Herein, the internal stress values calculated according to the shift in peak 1 from w_0 are shown in Table 1. PbCrO_4 obviously induced formation of compressive stress on oxide films at all oxidation times (1-20 min) because ΔW_γ was negative, although the internal tensile stress increased slightly according to ΔW_γ as the oxidation time increased from 10 to 20 min. This result can be explained by coupling of PbCrO_4 and PbO/PbO_2 peaks generated by the oxide films. With respect to the PbO/PbO_2 peak, Kanai *et al.* [21] previously reported PbO Raman bands at ~ 140.7 and $\sim 70.3\ \text{cm}^{-1}$, and a PbO_2 Raman band at $\sim 133.7\ \text{cm}^{-1}$, which corresponds to our band at $130\text{-}150\ \text{cm}^{-1}$ for PbO/PbO_2 . Because PbO was determined to be the main constituent of PbO by XRD (Fig. 2), the following internal stress results were calculated only considering PbO Raman frequency shifts. Based on the shift in peak 2, PbO was considered to obviously contribute to the internal tensile stress of the oxide film at a fixed oxidation time of 1 min.

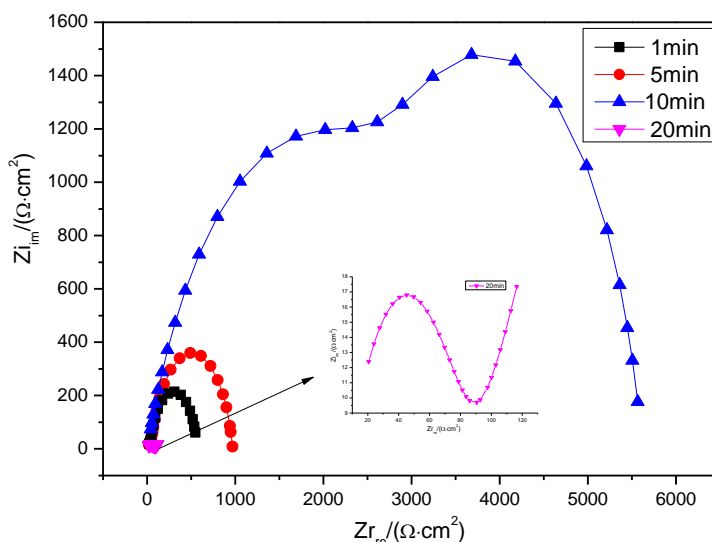


Figure 4. Electrochemical impedance diagrams for lead alloy surfaces treated in $1.5\ \text{mol}\cdot\text{L}^{-1}$ chromium (VI) solution at $40\ ^\circ\text{C}$ after 1, 5, 10, and 20 min of oxidation under the current density $20\ \text{A}\cdot\text{dm}^{-2}$.

As the oxidation time increased from 5 to 10 min, peak 2 exhibited a negative shift, and σ_{xx} represented compressive stress. However, peak 3 did not show significant movement. As the oxidation length increased from 10 to 20 min, both peaks 2 and 3 showed remarkable increases; internal tensile stress calculations are shown in Table 1. These results suggest that PbCrO_4 and PbO play an important role in determining internal stress formation during the initial oxidation process. Although PbCrO_4 compositions were found in XRD spectra and SEM, PbO and PbO_2 predominantly induced internal stress formation when oxidation time increased gradually. In addition, this indicates that coupling of

changes in compressive and tensile stresses seen in Table 1 encourages the dioxide layer to crack or break away from the lead substrate anode.

Fig. 4 shows electrochemical impedance diagrams for lead alloy surfaces treated with chromium (VI) under different conditions. The diagrams represent the electrical conductivity of oxide films in 3.5 wt% NaCl at room temperature. Over a 1-10 min oxidation period, the diagrams are characterized by one capacitive loop, and their charge transfer resistance (R_t , Nyquist curve diameter along the real axis) increased from ~ 549 to $\sim 5525 \Omega$. After 10 min of oxidation, the diagrams showed two capacitive loops at high and medium frequencies. It is interesting to note, however, the diagrams present a clear change after 20 min compared with other diagrams cases, showing one capacitive loop at both high and medium frequencies with a remarkably decreased R_t ($\sim 95 \Omega$) and low frequency Warburg impedance.

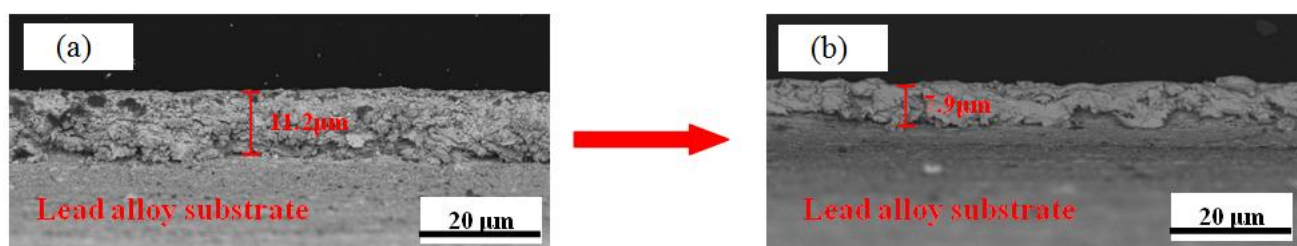


Figure 5. Cross-sectional SEM image of oxide films obtained in $1.5 \text{ mol}\cdot\text{L}^{-1}$ chromium (VI) solution at $40 \text{ }^\circ\text{C}$ under the current density $20 \text{ A}\cdot\text{dm}^{-2}$ after different oxidation times: (a) 10 min and (b) 20 min

According to Baril *et al.* [22], high and medium frequency loops are usually attributed to both charge transfer and a double layer associated with the interface between the electrolyte and alloy surface; the low frequency Warburg impedance is considered the ion's diffusion behavior. Thus, the above SEM, XRD, and Raman results indicate the electrical conductivity of oxide films obviously depends on the residual stresses and compositional change in oxide films. On the other hand, a higher monoclinic PbCrO_4 content increases R_t after 10 min of oxidation (Figs. 2 and 3). However, oxidations lasting longer than 10 min caused breaking and spalling of the oxide film due to inner stress changes, leading to a decrease in R_t and ion diffusion through the microcracks. In addition, cross-sectional SEM images of oxide films shown in Fig. 5 after oxidation times of 10 and 20 min also support these results, showing a decrease in film thickness from 11.2 to $7.9 \mu\text{m}$.

3.2 Effect of SO_4^{2-} ions on internal stress of oxide films on the surface of lead substrate anodes

As seen in Fig. 6 and Table 2, all Raman spectra obtained were composed of three peaks at 60-70, 140-150, and $960\text{-}980 \text{ cm}^{-1}$. As the oxidation time increased from 1 to 20 min, peak 1 shifted from 975.9 to 963.8 cm^{-1} , while peak 2 shifted from 140.2 to 147.8 cm^{-1} ; peak 3 showed a minor shift from 66.3 to 68.9 cm^{-1} over this time range (Fig. 6).

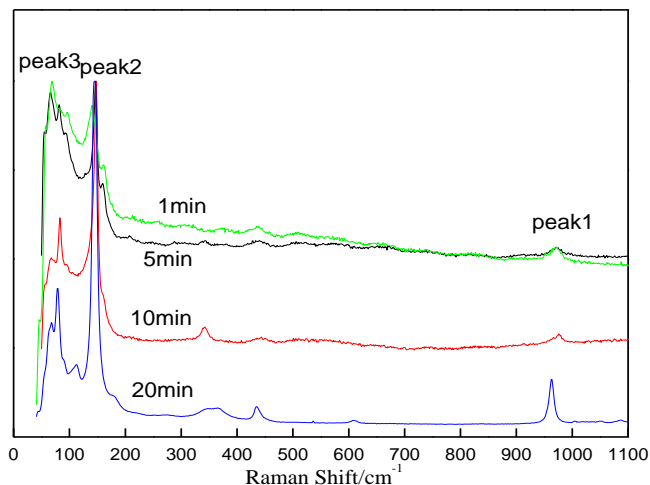


Figure 6. Raman spectra of lead alloy surfaces treated in 0.4 mol·L⁻¹ SO₄²⁻ solution at 40 °C after 1, 5, 10, and 20 min of oxidation under the current density 20 A·dm⁻².

Table 2. Raman peaks for lead alloy surfaces treated with 0.4 mol·L⁻¹ SO₄²⁻ solution at 40 °C after 1, 5, 10, and 20 min of oxidation under the current density 20 A·dm⁻².

Oxidation time(min)	Peak 1		Peak 2		Peak 3	
	Raman bands (cm ⁻¹)	Residual stresses(MPa)	Raman bands (cm ⁻¹)	Residual stresses(MPa)	Raman bands(cm ⁻¹)	Residual stresses(MPa)
0		-3.83		-3.83		--
1	975.9	-0.504	140.2	-0.105(for PbO)	68.9	--
5	973.1	-1.092	144.9	0.882(for PbO)	67.8	--
10	971.2	-1.491	146.7	1.260(for PbO)	66.3	--
20	963.8	-3.045	147.8	1.491(for PbO)	67.5	--

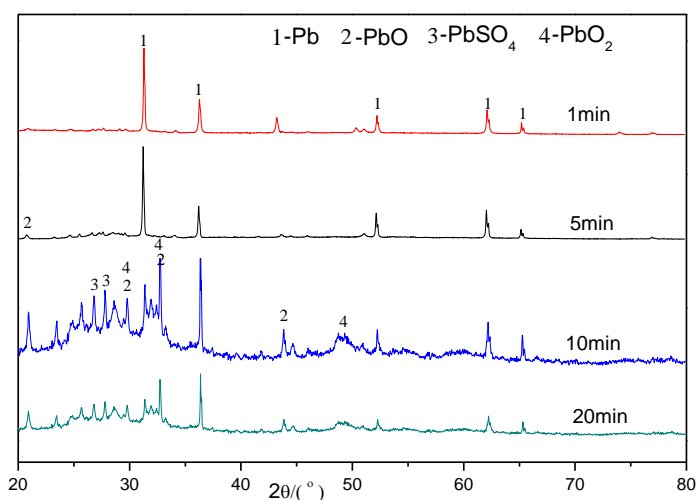


Figure 7. X-ray diffractograms of lead alloy surfaces treated in 0.4 mol·L⁻¹ SO₄²⁻ solution at 40 °C after 1, 5, 10, and 20 min of oxidation under the current density 20 A·dm⁻².

Corresponding XRD patterns and SEM at each oxidation time under the same conditions are presented in Figs. 7 and 8. As the oxidation time of the lead alloy in SO₄²⁻ solution increased, the lead

diffraction peaks apparently weakened, while those of PbO/PbO₂ were strengthened remarkably. For PbO/PbO₂ mix films, the PbO also keeps the main component. However, PbSO₄ diffraction peaks were relatively strong after 10 and 20 min oxidations versus 1 and 5 min. According to surface morphology, the cube-shaped grains formed on the lead alloy surface gradually grew in size (Fig. 8). Moreover, the ball-shaped grains gradually covered the cube-shaped grains and grains size were gradually grown up. This indicates that the oxide film initially consisted of PbO/PbO₂, and then PbO and monoclinic PbSO₄ gradually formed with a small amount of PbO₂.

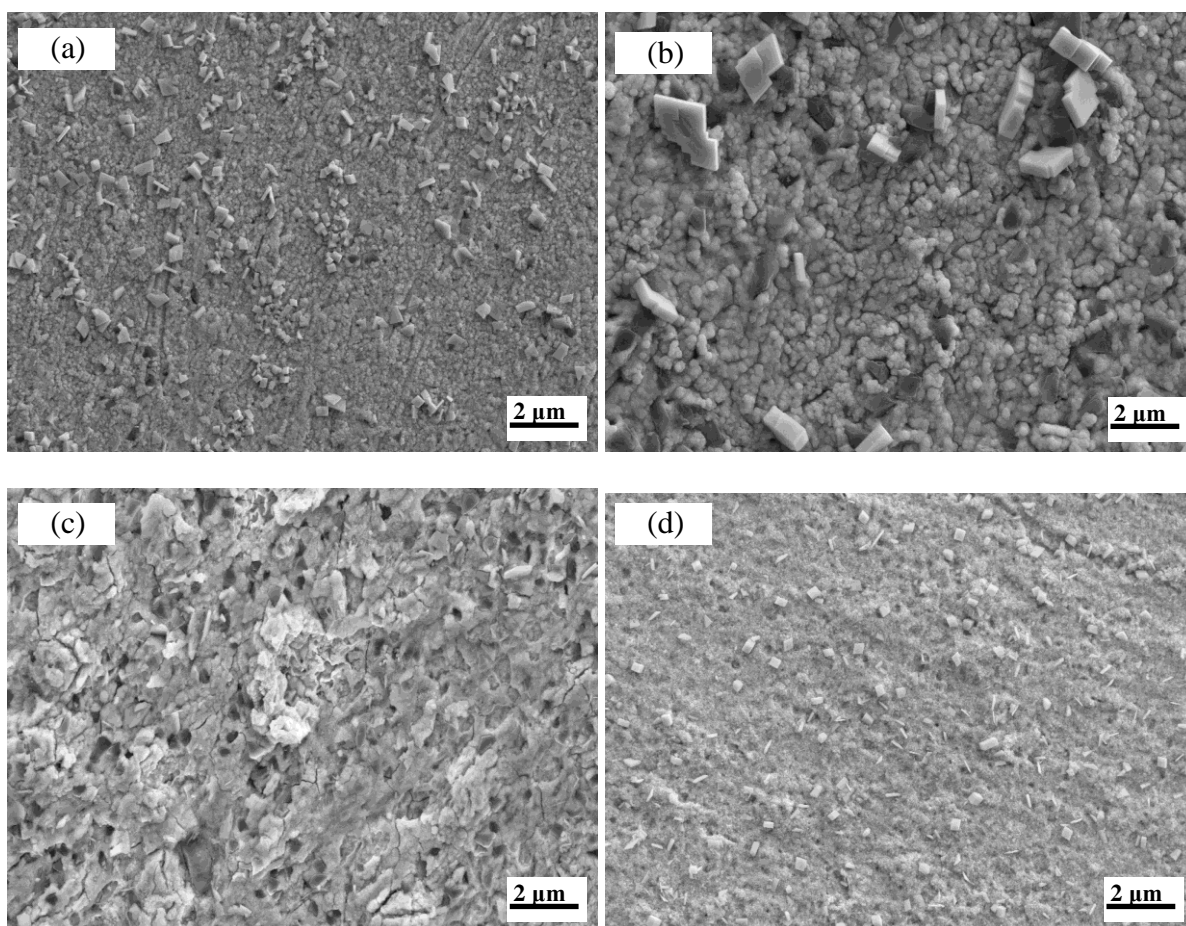


Figure 8. Surface morphology of lead alloy treated in 0.4 mol·L⁻¹ SO₄²⁻ solution at 40 °C after different oxidation time under the current density 20 A·dm⁻²: (a) 1 min, (b) 5 min, (c) 10 min, and (d) 20 min

Compared to the Raman spectra shown in Fig. 1, Raman peak positions in Fig. 6 are fixed at 960-980 cm⁻¹, indicating the presence of PbSO₄. According to the theoretical analysis of the above internal stresses and results, the ΔW_γ values of PbSO₄ corresponding to peak 1 were negative over the entire 20 min oxidation period; therefore, σ_{xx} exhibits compressive stress. As shown in Table 2, the absolute value of each stress increased with increased oxidation time and reached 3.045 MPa after 20 min. On the contrary, the ΔW_γ values of PbO (not considering PbO₂ due to their low composition) corresponding to peak 2 were positive and increase over the entire 20 min oxidation period. Thus, σ_{xx} was attributed to tensile stress. It is interesting to note, however, that the stress value for PbO oxide

films increased to 1.491 MPa after 20 min. These internal stress results demonstrate that microstructural changes due to oxide film composition leads to internal stress formation and changes.

Electrochemical impedance diagrams illustrate the change in electrical conductivity of oxide films on lead alloy surfaces in SO_4^{2-} solution under different conditions (Fig. 9). A 1 min oxidation was characterized by one capacitive loop and one Warburg impedance line due to the thin oxide film obtained at the initial oxidation stage, and ion diffusion reactions were easily induced.

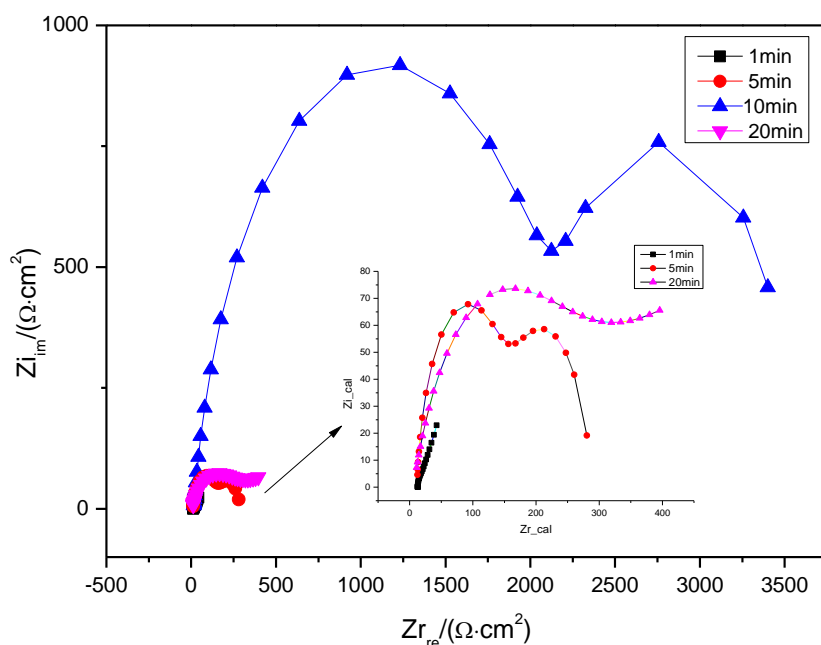


Figure 9. Electrochemical impedance diagrams for lead alloy surfaces treated in $0.4 \text{ mol}\cdot\text{L}^{-1} \text{SO}_4^{2-}$ solution at $40 \text{ }^\circ\text{C}$ after 1, 5, 10, and 20 min of oxidation under the current density $20 \text{ A}\cdot\text{dm}^{-2}$.

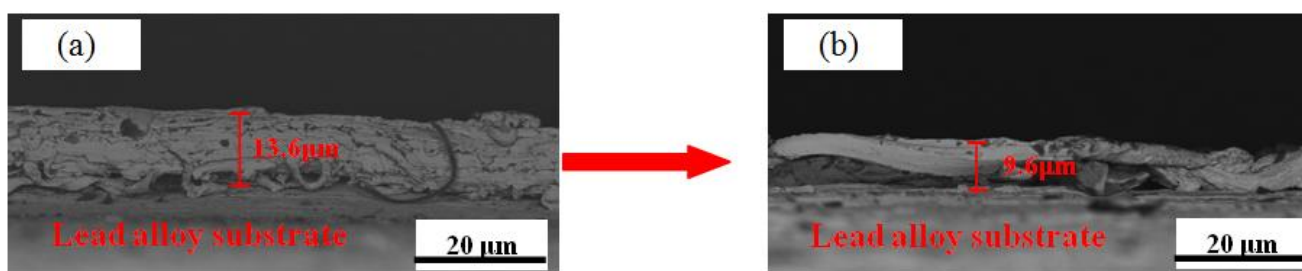


Figure 10. Cross-sectional SEM image of oxide films obtained in $0.4 \text{ mol}\cdot\text{L}^{-1} \text{SO}_4^{2-}$ solution at $40 \text{ }^\circ\text{C}$ under the current density $20 \text{ A}\cdot\text{dm}^{-2}$ after different oxidation times: (a) 10 min; (b) 20 min.

From 5 to 20 min, the diagrams tended to resemble those of the CrO_3 solution. The difference is that the PbSO_4 composition substitutes for the monoclinic PbCrO_4 seen by XRD and has a clear effect on electrical conductivity and film thickness. The diagrams show two capacitive loops at high and medium frequencies, and their R_t increased from ~ 289 to $\sim 3500 \text{ } \Omega$ from 5 to 10 min. After 20 min, the R_t decreased and one Warburg impedance line was observed. The reason for these results is similar to that for oxide films obtained in CrO_3 solution, which can be partly attributed to oxide film spalling

at oxidations lasting longer than 10 min. These results are also shown in Fig. 10, where film thickness decreased from 13.6 to 9.6 μm at 10 and 20 min, respectively.

3.3 Effect of Cl^- ions on internal stress of oxide films on the surface of lead substrate anodes

As seen in Fig. 11 and Table 3, spectra of all samples are composed of two peaks fixed at 60-70 and 130-160 cm^{-1} . As the oxidation time increased from 1 to 20 min, peak 2 shifted from 135.5 to 160.6 cm^{-1} . Peak 3 remained virtually unchanged at 67.8 cm^{-1} from 1 to 5 min and then decreased to 64.0 cm^{-1} from 5 to 10 min; after 20 min, peak 3 remained fixed at 65.1 cm^{-1} . The corresponding XRD patterns and SEM at each oxidation time are shown in Figs. 12 and 13. As the oxidation time of the lead alloy in Cl^- solution increased, lead diffraction peaks obviously weakened, while those of PbO/PbO_2 were strengthened remarkably.

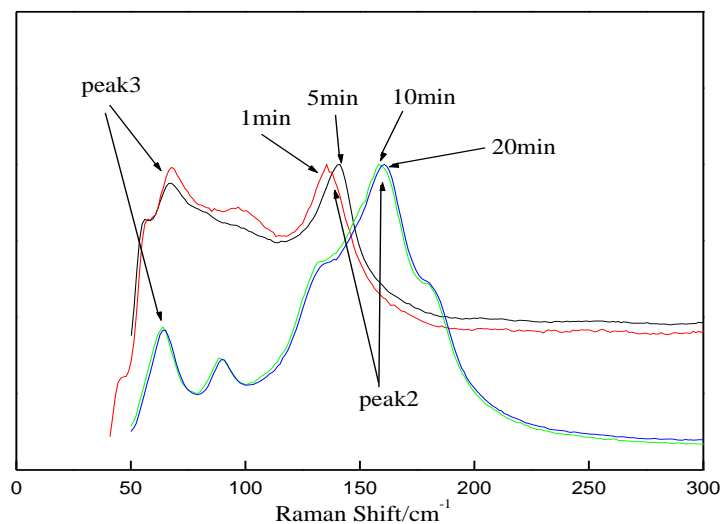


Figure 11. Raman spectra of lead alloy surfaces treated in 1.0 mol·L⁻¹ Cl^- solution at 40 °C after 1, 5, 10, and 20 min of oxidation under the current density 20 A·dm⁻².

Table 3. Raman peaks for lead alloy surfaces treated with 1.0 mol·L⁻¹ Cl^- solution at 40 °C after 1, 5, 10, and 20 min of oxidation under the current density 20 A·dm⁻².

Oxidation time(min)	Peak 2		Peak 3	
	Raman bands (cm^{-1})	Residual stresses(MPa)	Raman bands (cm^{-1})	Residual stresses(MPa)
0		-3.83		--
1	135.5	-1.092(for PbO)	67.8	--
5	141.4	0.147(for PbO)	67.8	--
10	158.3	3.696(for PbO)	64.0	--
20	160.6	4.179(for PbO)	65.1	--

In addition, Pb(OH)Cl diffraction peaks were relatively strong for 10 and 20 min oxidations compared to those at 1 and 5 min. According to surface morphology, black hole-shaped grains formed

on the lead anode surface after 1 min (Fig. 13). At the same time, thin, ball-shaped grains gradually grew in size, especially after 5 min of oxidation. After 10 min, the block-shaped grains gradually covered the substrate surface, and thin and acicular crystals were found on the surface of the block-shaped grains. This can be explained by PbCl_2 being generated on the substrate surface during the initial oxidation process, which may represent dissolution of PbCl_2 in the electrolyte since it is a microsoluble compound, thus leading to the black hole-shaped formation seen in Fig. 13. As the oxidation time increased, PbO/PbO_2 oxide film gradually grew and covered the substrate surface and had better corrosion resistance than PbCl_2 . After 10 min, Cl^- ions showed a remarkable reaction with PbO/PbO_2 and OH^- ions, leading to Pb(OH)Cl formation on the oxide film surface. This is in accordance with the fact that lead and PbO/PbO_2 crystals are mainly found during initial oxidation, while PbO/PbO_2 and Pb(OH)Cl crystals without lead are dominant in oxide films after 10 min of oxidation, according to the above XRD results.

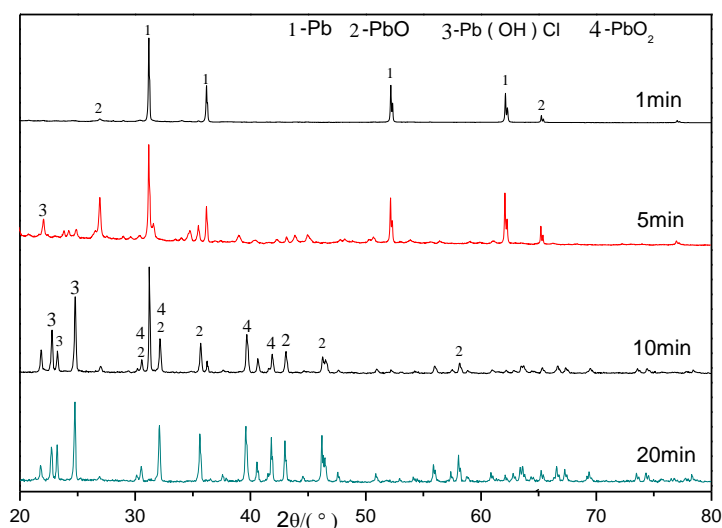
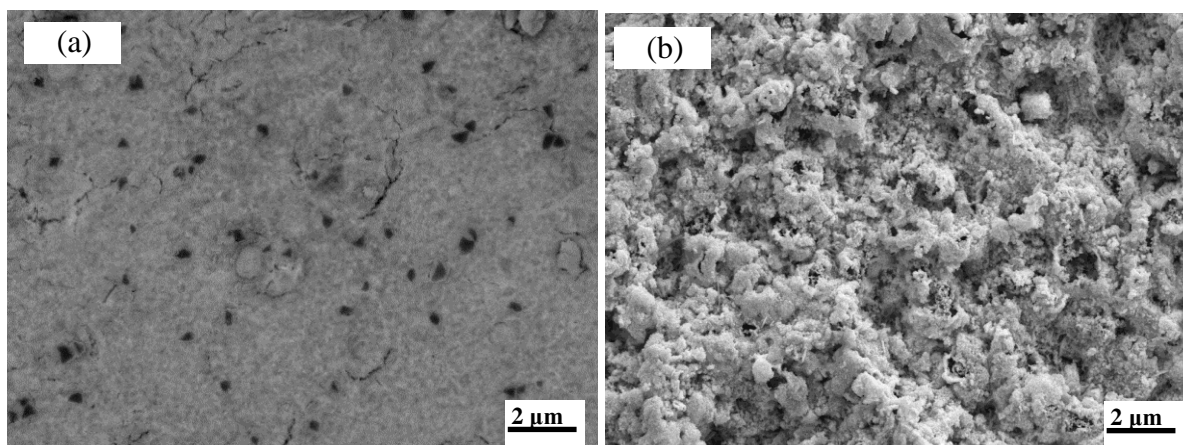


Figure 12. X-ray diffractograms of lead alloy surfaces treated in $1.0 \text{ mol}\cdot\text{L}^{-1} \text{ Cl}^-$ solution at $40 \text{ }^\circ\text{C}$ after 1, 5, 10, and 20 min of oxidation under the current density $20 \text{ A}\cdot\text{dm}^{-2}$.



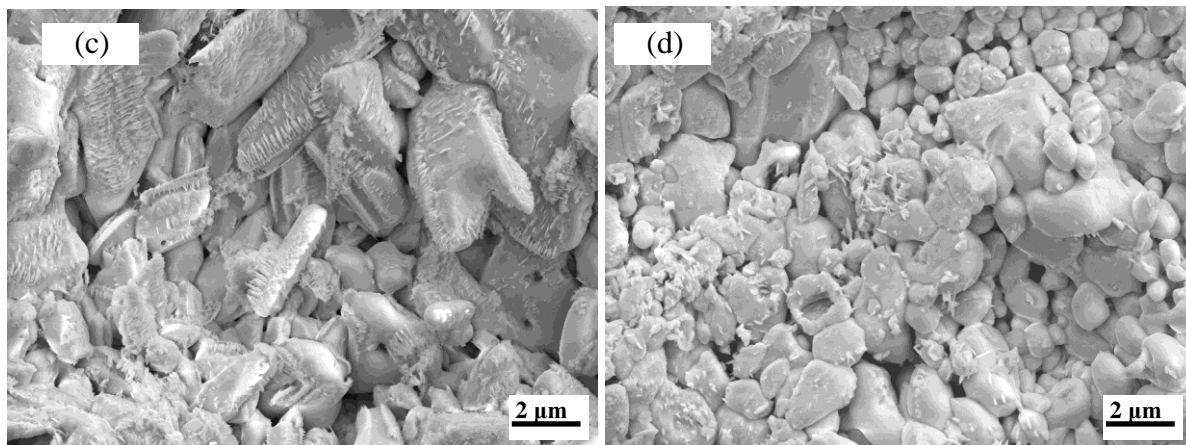


Figure 13. Surface morphology of lead alloy surfaces treated in 1.0 mol·L⁻¹ Cl⁻ solution at 40 °C after different oxidation time under the current density 20 A·dm⁻²: (a) 1 min, (b) 5 min, (c) 10 min, and (d) 20 min

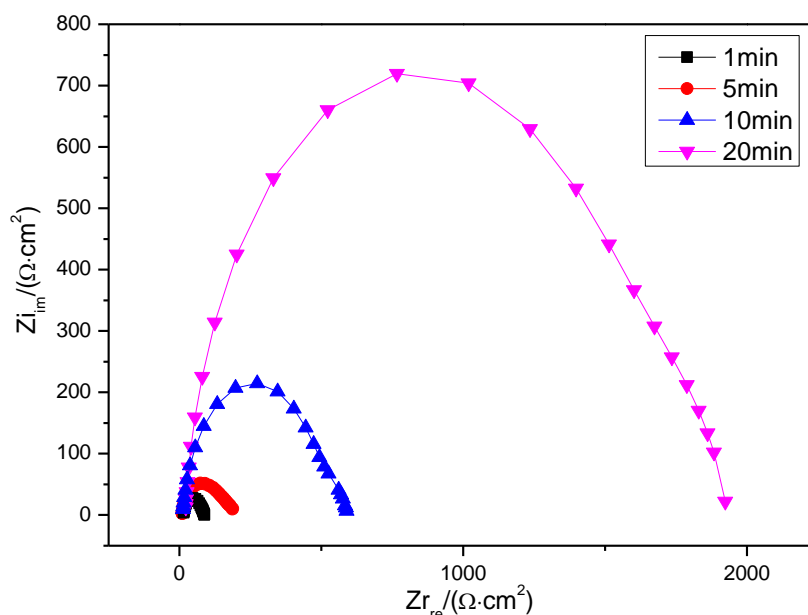


Figure 14. Electrochemical impedance diagrams for lead alloy surfaces treated in 1.0 mol·L⁻¹ Cl⁻ solution at 40 °C after 1, 5, 10, and 20 min of oxidation under the current density 20 A·dm⁻².

According to the theoretical analysis of the above internal stresses and results, the ΔW_γ values of PbO (not considering PbO₂ due to their low composition) corresponding to peak 2 were positive in the oxidation period from 1 to 5 min; therefore, σ_{xx} represents tensile stress; calculated stresses values are summarized in Table 3. As the oxidation time increased from 5 to 20 min, Raman peaks to 158.3 and 160.6 cm⁻¹, respectively, and all were above the 140.7-cm⁻¹ PbO Raman band defined by Kanai *et al.* [21]. This implies that the Pb(OH)Cl phase is critical for inducing positive Raman peak shifts. As a result, internal stresses of σ_{xx} obviously increased from -1.092 to 4.179 MPa, showing tensile stress. Furthermore, the Raman shift for peak 3 exhibited an insignificant change.

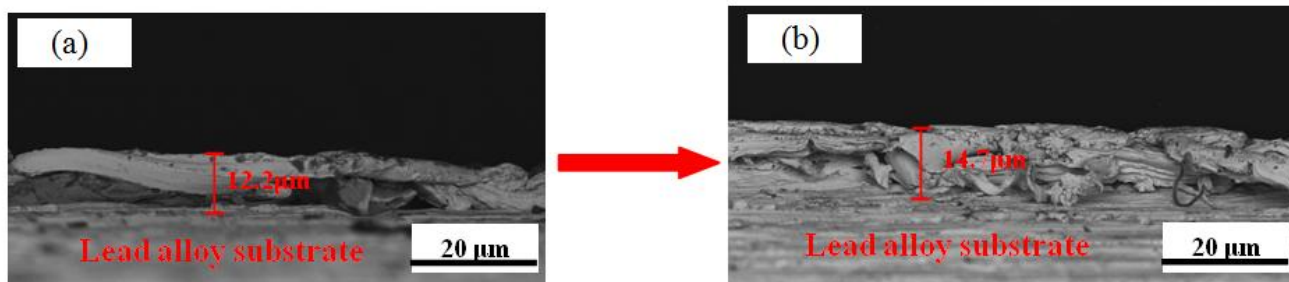


Figure 15. Cross-sectional SEM image of oxide films obtained in $1.0 \text{ mol}\cdot\text{L}^{-1} \text{ Cl}^-$ solution at $40 \text{ }^\circ\text{C}$ under the current density $20 \text{ A}\cdot\text{dm}^{-2}$ after different oxidation times: (a) 10 min and (b) 20 min

Compared to the other electrolyte solutions, electrochemical impedance diagrams for oxide films obtained in Cl^- ion solutions were characterized by one capacitive loop in all diagrams (Fig. 14). Furthermore, the R_f increased from ~ 186 to $\sim 1930 \text{ } \Omega$ from 1 to 20 min due to the gradual growth of film thickness (Fig. 15), indicating a decrease in electrical conductivity. This is the result of the transformation of some PbO to $\text{Pb}(\text{OH})\text{Cl}$, which was a fine, needle-like, crystalline grain generated on the PbO crystalline grain surface seen in Fig. 13. Consequently, the oxide films showed no significant changes in lattice volume or microcracks.

4. CONCLUSIONS

In the current study, lead diffraction peaks were found on the substrate anode surface using different ion solutions as electrolytes at the initial oxidation stage. With increasing oxidation duration, lead diffraction peaks were weakened, while those of PbO/PbO_2 strengthened remarkably. Monoclinic PbCrO_4 , PbSO_4 , and $\text{Pb}(\text{OH})\text{Cl}$ diffraction peaks were also generated by oxide films grown in chromium(VI), SO_4^{2-} , and Cl^- solutions, respectively. Raman spectral results revealed that the all PbO/PbO_2 peaks at $130\text{-}140 \text{ cm}^{-1}$ or $\sim 70.3 \text{ cm}^{-1}$ were observed with all three ion solutions, and PbCrO_4 peaks at $830\text{-}840 \text{ cm}^{-1}$ were found using the chromium(VI) electrolyte. PbCrO_4 and PbO/PbO_2 induced compressive stresses which change obviously from 1 to 5 min of oxidation, while internal stresses changed to tensile stresses after 10 to 20 min. PbSO_4 peaks at $960\text{-}980 \text{ cm}^{-1}$ were generated in the SO_4^{2-} solution and were considered to represent compressive stresses on the oxide film due to the negative shift. In addition, PbO/PbO_2 films obtained in SO_4^{2-} solution were attributed to tensile stresses because of the positive peak shift. As for the Cl^- solution, $\text{Pb}(\text{OH})\text{Cl}$ in oxide films induced positive PbO/PbO_2 peak shifts above 140 cm^{-1} , which induced the tensile stresses on oxide films. Overall, coupling changes in compressive and tensile stress caused the dioxide layer to crack and even break away from the lead alloy anode, thereby increasing the electrical conductivity of the oxide films.

ACKNOWLEDGMENTS

This work was financially supported by the National Natural Science Foundation of China (51374053) and the Special Fund for Basic Scientific Research of Central Colleges (N130502002).

References

1. X. Li, D. Pletcher, F.C. Walsh, *Chem. Soc. Rev.*, 40 (2011) 3879.
2. D. Devilliers, M. T. Dinh Thi, E. Mahé, Q. L. Xuan, *Electrochim Acta*, 48(2003) 4301.
3. N. Li, J. S. Zhang, B. H. Sencer, D. Koury, *Nucl. Instrum. Methods Phys. Res., Sect. A*, 562(2006), 695-697.
4. D. R. P. Egan, C. T. J. Low, F. C. Walsh, *J. Power Sources*, 196(2011) 5725.
5. W. R. O'sorio, L. C. Peixoto, A. Garcia, *J. Power Sources*, 194(2009) 1120.
6. Y. Li, L. X. Jiang, X. J. Lv, Y. Q. Lai, H. L. Zhang, J. Li, Y. X. Liu, *Hydrometallurgy*, 109 (2011) 252.
7. A. M. Lafront, W. Zhang, E. Ghali, G. Houlachi, *Electrochim Acta*, 55(2010) 6665.
8. I. Ivanov, Y. Stefanov, Z. Noncheva, M. Petrova, Ts. Dobrev, L. Mirkova, R. Vermeersch, J.-P. Demaerel, *Hydrometallurgy*, 57(2000) 109.
9. F. A. Pérez-González, C. G. Camurri, C. A. Carrasco, R. Colás, *Mater. Charact.*, 64(2012) 62.
10. S.E. Doyle, M.E. Herron, K.J. Roberts, J. Robinson, F.C. Walsh, *Phase Transitions*, 39(1992) 135.
11. C. Ponce de León, F.C. Walsh, *Surf. Coat. Tech.*, 259 (2014) 676.
12. F. Hine, K. Takayasu, N. Koyanagi, *J. Electrochem. Soc.*, 133, 346 (1986).
13. V.C. Nguyen, C.Y. Lee, F.J. Chen, C.S. Lin, T.Y. Liu, *Surf. Coat. Tech.*, 206 (2012) 3201.
14. S.Y. Chang, U. Krupp, H.-J. Christ, *Mater. Sci. Eng., A*, 301(2001) 196.
15. S. Pyun, *Mater. Lett.*, 27(1996) 297.
16. Z. Sunny, K. S. Apurbba, *Surf. Coat. Tech.*, 291 (2016) 413-422.
17. J.-F. Vanhumbecq, J. Proost, *Electrochim Acta*, 53(2008) 6165.
18. T. Kociniewski, J. Moussodji, Z. Khatir, *Microelectron. Reliab.*, 54 (2014) 1770.
19. J. Gleize, M.A. Renucci, J. Frandon, E. Bellet-Amalric, B. Baudin, *J. Appl. Polym.*, 93(2003) 2065.
20. J.Z. Li, X.L. Sun, Y.W. Tian, Y. Zhao, *J. Electrochem. Soc.*, 160(2013)E60.
21. H. Kanai, Y. Yamashita, M. Kakihanab, M. Yoshimurab, *J. Eur. Ceram. Soc.*, 16(1996)1157.
22. G. Baril, C. Blanc, M. Keddam, N. Pébère, *J. Electrochem. Soc.*, 150 (2003) B488.

© 2016 The Authors. Published by ESG (www.electrochemsci.org). This article is an open access article distributed under the terms and conditions of the Creative Commons Attribution license (<http://creativecommons.org/licenses/by/4.0/>).